PCCP

PAPER

View Article Online
View Journal | View Issue

Cite this: *Phys. Chem. Chem. Phys.*, 2023, **25**, 11555

Impact of the Si/Al ratio on the ethanol/water coadsorption on MFI zeolites revealed using original quantitative IR approaches†

Rita Zakhia Douaihy, Louwanda Lakiss, Mohamad El-Roz, Yoann Levaque, Alexandre Vimont and Philippe Bazin *

Received 3rd February 2023,
Accepted 28th March 2023

DOI: 10.1039/d3cp00549f

rsc.li/pccp

Advanced IR vibrational spectroscopic techniques, *e.g.*, using a coupled gravimetric-IR surface analyzer (AGIR) and a high-throughput *in situ* IR cell (Carroucell), have been used for the quantitative studies of the adsorption and coadsorption of ethanol and water on MFI zeolites with different Si/Al ratios. The AGIR coupling is a powerful tool for the accurate determination of the molar adsorption coefficients during coadsorption experiments since their evaluation is based on the measurement of the exact amount of adsorbed species. The use of the Carroucell set up allows characterizing all the samples simultaneously, strictly in the same gaseous and temperature environment. The molar absorption coefficients of pure adsorbed ethanol and water are determined: their values are constant whatever the Si/Al ratio of the MFI zeolites. Moreover, these coefficients are found to be identical in the case of the water–ethanol coadsorption experiments. Their use allows obtaining the exact quantity of each adsorbate specie in the binary system. At low partial pressures, the unary water adsorption experiments suggest that the amount of adsorbed water results mainly from the preferential adsorption on Brønsted acid sites in tetrameric clusters. In contrast, the adsorption of EtOH occurs on both silanol groups and Brønsted acid sites (BASs). The effect of the Si/Al ratio is only observed at relatively low partial pressures. The effect of the Si/Al ratio on the ethanol adsorption capacity is also investigated. This study directs the choice of an appropriate zeolite once it is used in membranes for drying ethanol.

1. Introduction

The recent energy and climate crises have pushed researchers to find alternatives for fossil fuels.[1] Countries have shifted to environmentally friendly and more efficient biofuels to minimize the extraction of fossil fuels and greenhouse gases.[2,3] In this context, bioethanol has gained significant interest due to its nature as a liquid phase, its use as a partial replacement for gasoline, and its facile transportation.[4–6] It can be produced from different sources ranging from food renewable sources such as corn starch and sugarcanes to non-food renewable sources, including the organic fraction of municipal solid waste and lignocellulosic biomasses.[7,8] Several techniques are applied to synthesize bioethanol; yet, the main challenge is separating ethanol from an ethanol/water mixture.[9] Bioethanol should be anhydrous to be used as a replacement for gasoline.[6,10] On an industrial scale, conventional distillation and separation processes are considered costly, energy intensive, and time-consuming due to the necessity to overcome the azeotrope barrier.[11] Therefore, other separation methods (pervaporation,[12] *etc.*) were elucidated to separate ethanol–water mixtures beyond the azeotropic mixture based on the adsorption on porous materials,[10,13] such as zeolites. Zeolites are widely used in catalysis, adsorption, and the separation of gaseous mixtures and biotechnologies,[14–16] due to their high tunable porosity, tunable characteristics, and high chemical and thermal stabilities, which make them excellent candidates for water/ethanol separation.[14,17] Therefore, the adsorption of ethanol (EtOH) on zeolitic materials has been extensively studied using experimental or theoretical approaches.[10,18–27] Siliceous zeolites with high silica contents present high selectivity for alcohols toward water in contrast to zeolites with higher alumina contents.[21,28] MFI zeolites have attracted attention due to the possibility of varying the aluminum content easily during the synthesis, allowing for tuning the hydrophobic/hydrophilic properties.[29] The organophilic nature of MFI zeolites was confirmed by Gómez-Álvarez *et al.*[30] and Zhang *et al.*[31] They concluded that no matter the Si/Al ratio of the MFI zeolites, the same behavior towards ethanol can be observed. This was not the case when adsorbing water, where water

Normandie Universite, ENSICAEN, UNICAEN, CNRS, Laboratoire Catalyse et Spectrochimie, 14050 Caen, France. E-mail: philippe.bazin@ensicaen.fr

† Electronic supplementary information (ESI) available. See DOI: https://doi.org/10.1039/d3cp00549f

uptake decreased with the increase of the Si/Al ratio.[32] From an experimental point of view, different techniques of characterization were implemented to study the adsorption and coadsorption of water and/or alcohols on porous materials such as gravimetry and volumetry,[33] *in situ* infrared spectroscopy,[13] nuclear magnetic resonance (NMR) with a pulsed-field gradient (PFG) and spin relaxation methods.[31,34–38] These methods coupled or not with theoretical calculations allow identifying the nature of the species adsorbed on the surface of the material.[27,39,40] Among them, IR spectroscopy can be a suitable technique to determine the nature and the quantities of adsorbed species[41,42] during vapor phase sorption experiments, mainly in transmission mode but in some cases using diffuse reflectance accessories.[43,44] In particular, a powerful investigation tool to access qualitative and quantitative data during unary and binary sorption experiments is a home-made coupled IR-gravimetry setup (namely AGIR).[13,45–47] This apparatus, working in transmission mode, allowed us determining the molar absorption coefficients (ε) of some specific infrared bands of the adsorbed species and then determining the concentration of the adsorbed species, as demonstrated during water and ethanol coadsorption on a MOF material at large vapor phase concentrations (P/P_0 = 0.006–0.65).[13]

However, one of the experimental limitations during coadsorption experiments on porous materials is the long delay to reach the sorption equilibrium state. Quantifying each coadsorbate after equilibration could be very challenging when measurements are performed on extended mixed vapor phase concentration ranges, all the more so the series of adsorbent samples investigated were large.[48] This is one of the reasons why the experimental data relative to water/alcohol coadsorption experiments (selectivity) are scarce and limited to a series of few samples.[30,33]

Recently, a new multi-sample *in situ* infrared cell was designed (namely Carroucell). It was developed to analyze simultaneously up to 12 samples strictly under the same experimental pressure and temperature conditions.[45] The set up has been validated using a set of quantitative data relative to pyridine sorption achieved in a reasonable time-acquisition on an extended series of zeolitic materials. This study demonstrates the possibility of using such a high throughput infrared setup as a fast-screening tool for the assessment and evaluation of the vapor phase sorption properties of adsorbents.

The aim of this work is to demonstrate, in the context of coadsorption experiments on porous materials, the relevance of combining the use of a home-made coupled IR-gravimetry setup (AGIR) with the implementation of a multi-sample *in situ* IR cell (Carroucell). First, through the AGIR system, the molar absorption coefficients (ε) of some specific IR bands of adsorbed water and ethanol on a series of MFI zeolites were determined. Then, the relative ethanol and water affinities of a series of protonic MFI zeolites with Si/Al ratios ranging from 11 to an infinite value (purely siliceous silicalite) were evaluated by the coadsorption of water and ethanol vapor phase in a large concentration range (P/P_0 = 0.006–0.65) using the Carroucell system according to a high-throughput approach. The sets of quantitative coadsorption data, recorded in a reasonable time-acquisition and with a good experimental resolution, are therefore very suitable for the demonstration of a potential effect of the acid properties of the zeolite materials modulated using the Si/Al ratio on their water–ethanol adsorption/separation performances.

2. Experimental section

2.1. Materials

A series of MFI zeolites with different Si/Al ratios were used in this work. The MFI-X systematic notation was used to name the zeolitic materials with X for the Si/Al molar ratio. Silicalite-1 was provided by Lakiss *et al.* and synthesized according to the procedure described in ref. 49; MFI-75 and MFI-38 were synthesized according to the procedure described in ref. 50; MFI-45 was a commercially synthesized zeolite by Clariant (formerly Süd Chemie); MFI-25 was synthesized according to Qin *et al.*'s work reported in ref. 51. and MFI-15 and MFI-11 were provided by IFP, synthesized without a template, and in the presence of pre-synthesized germinal zeolites, respectively.

2.2. Characterization techniques

The PXRD patterns of the zeolites were recorded using a PANalytical X'Pert Pro diffractometer with an average Cu Kα radiation (λ = 1.5418 Å). The θ–2θ scans were recorded in the range of 2θ between 5° and 50° and a step size of ~0.0167°.

The Si/Al ratio was determined from the elemental analysis using inductively coupled plasma spectroscopy coupled with mass spectrometry. The powder was dissolved in a mixture of aqua regia (HCl + HNO_3) and hydrofluoric acid (HF) at 90 °C. HF was then neutralized using boric acid (H_3BO_4). The mass spectrum of the diluted analyte solution was recorded after ionizing the solution with a high-energy Ar-plasma.

Nitrogen sorption isotherms at 77 K were recorded using a Micrometrics ASAP 2020 volumetric adsorption analyzer after degassing the samples at 350 °C for 12 hours. The specific surface areas were determined from the BET equation. The total pore volumes and the external surface areas were calculated using the *t*-plot method.

The morphology of zeolite crystals was investigated using scanning electron microscopy (SEM). SEM images were recorded using a TESCAN Mira field-emission scanning microscope at 20 kV. Before recording the images, the powder was dispersed on carbon tape and coated with platinum.

2.3. *In situ* IR spectroscopy

For the determination of acidic properties using the classical IR *in situ* approach, self-supported pellets of pressed powder of each zeolite (~20 mg, 10^7 Pa cm^{-2}, S = 2.0 cm^2) are mounted in an *in situ* IR cell equipped with KBr windows connected to a Nicolet 6700 IR spectrophotometer. The spectrometer is equipped with a DTGS detector and an extended-KBr beam splitter. IR spectra were recorded in the region between 400 and 5500 cm^{-1} at a resolution of 4 cm^{-1} and 128 scans per spectrum.[45] The *in situ* IR cell used in this work is the

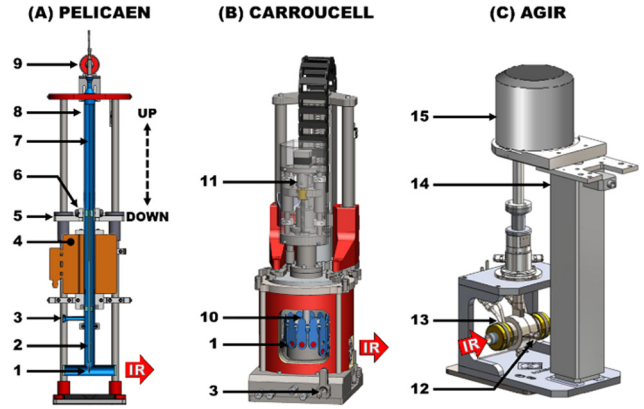

Fig. 1 General views of the IR cells: (A) PELICAEN used for the acidity evaluation, (B) Carroucell used for coadsorption measurements and (C) AGIR used for the molar absorption coefficient determination. 1 – sample (disc 16 mm), 2 – sample holder, 3 – connection to the vacuum/gas flow apparatus, 4 – oven, 5 – motorized stage (the sample is at IR beam (DOWN) or an oven (UP) level), 6 – magnetic suspension, 7 – thermocouple, 8 – quartz tube, 9 – pressure gauge, 10 – carrousel with 12 positions, 11 – motorized translation and rotation units, 12 – connection to the gas flow, 13 – IR cell reactor, 14 – telescopic column, and 15 – setaram microbalance head.

PELICAEN cell (Fig. 1(A)) which is the latest version developed by the LCS laboratory to improve the sample temperature control and automate the main functions (the change of positions of the sample from an oven to the IR beam and the acquisition of the IR spectra). The PELICAEN cell is mainly made of quartz. The sample holder is designed with a platinum wire. The heating system (up to 700 °C) is a tubular furnace from ERALY (France). A thermocouple is positioned inside the cell near the sample to perfectly control its temperature, particularly when placed under vacuum (low thermal conductivity conditions). An additional gauge is added to the IR cell to precisely measure the pressure inside the chamber. For the IR spectroscopic evaluation of the properties of porous materials, the addition of probe molecules can also be done gradually and quantitatively *via* a small, calibrated volume (approximately 2.0 cm^3) positioned at the front side of the cell. The PELICAEN cell is connected to the vacuum apparatus to treat the sample and introduce the gaseous phase when necessary. In this work, zeolites were activated at 400 °C (heating rate 2 °C min^{-1}) under vacuum (around 10^{-5} torr) for 5 hours.

2.4. Method for the determination of the molar absorption coefficients of adsorbed ethanol and water

The AGIR technique (Fig. 1(C)) allows measuring the gravimetric data and records the corresponding IR spectra simultaneously.[13,45,47] Therefore, the AGIR technique is very well suited to determine the molar absorption coefficients of the bands associated with the vibration modes of the adsorbed molecules. Note that these coefficients are essential for quantitative investigations. The setup is connected to a mass spectrometer to monitor the outlet flow of the adsorbates in the gas phase (Pfeiffer Omnistar GSD301). The experiments were conducted on a self-supported pellet of the pressed powder of the adsorbent (~20 mg, 10^7 Pa cm^{-2}, S = 2.0 cm^2), previously activated at 400 °C (heating rate 0.6 °C min^{-1}) under a gas flow (20 cm^3 min^{-1}) of a mixture of argon and oxygen (20%). IR spectra were recorded using a Nicolet 6700 spectrometer outfitted with a liquid nitrogen cooled MCT detector (mercury, cadmium, and tellurium detector) at a resolution of 4 cm^{-1} in the spectral region between 600 cm^{-1} and 6000 cm^{-1}. The mass of the sample was recorded using a microbalance (accuracy = 0.1 μg), and the corresponding IR spectra were recorded after the equilibrium state of H_2O and EtOH concentrations. The steady state was determined by both the absence of change in mass and the intensity of the characteristic band of each adsorbate.

2.5. Adsorption and coadsorption of ethanol and water using the Carroucell high-throughput IR cell

To drastically reduce the experimental time due to the high number of samples and different partial pressure points of H_2O and C_2H_5OH, the coadsorption measurements were carried out using the Carroucell apparatus.[45] This sophisticated IR apparatus developed in the laboratory (Fig. 1(B)) allows simultaneously performing under the same experimental conditions on twelve samples (all samples are placed in the same analysis chamber). The setup is made of an *in situ* IR cell, attached to a vacuum system, and adapted for 12 samples of self-supported pellets formed of a pressed powder (~20 mg, 10^7 Pa cm^{-2}, S = 2.0 cm^2). The background and the gas phase spectra are recorded before each sample measurement and are automatically subtracted. In this work, the Carroucell is adapted for experiments under a gas flow, so experimental conditions are similar to that of the AGIR setup. Upstream of the adsorption sequences, the zeolites are activated at 400 °C under an argon flow. First, a water concentration was introduced to the cell at RT, followed by the adsorption of increasing ethanol concentrations after reaching equilibrium. The equilibrium after ethanol and water adsorption is determined between two consecutive IR spectra, where no change in the characteristic vibrational bands of the adsorbates is observed. The coadsorption experiments were conducted at 25 °C at different water concentrations, ranging between P/P_0 = 0.016 and 0.64. As for the partial pressure of ethanol, it increases from 0.006 to 0.65.

3. Results and discussion

3.1. Structural and textural properties

The textural porosities of the zeolites are investigated using nitrogen adsorption/desorption isotherms and are summarized in Table 1 after determining their Si/Al ratio and confirming their purity from the PXRD patterns, where the main characteristic peaks of the MFI structure are present on all the patterns without any additional peaks (Fig. S1(A), ESI†). The N_2 isotherms are shown in Fig. S1(B) (ESI†) and correspond to type I isotherms, the characteristic of microporous zeolites.[52] The BET surface areas and the micropore volumes of different zeolites vary in the same range. Zeolites are then characterized

Table 1 Si/Al ratios[a], textural properties[b] and accessibility of acid sites of different MFI zeolites

	Silicalite	MFI-75	MFI-45	MFI-38	MFI-25	MFI-15	MFI-11
Si/Al ratio[a]	∞	75	45	38	25	15	11
S_{BET}[c] ($m^2\ g^{-1}$)	502	421	452	423	475	413	444
Micropore volume[d] ($cm^3\ g^{-1}$)	0.158	0.157	0.153	0.155	0.156	0.166	0.162
External surface area[c] ($m^2\ g^{-1}$)	138	76	77	89	125	29	57
Number of Al per unit cell	0	1.3	2.1	2.5	3.7	6.0	8.0
n Lewis acid sites[e] ($\mu mol\ g^{-1}$)	0	12	44	46	48	51	34
n BAS[f] ($\mu mol\ g^{-1}$)	0	145	190	157	270	524	712

[a] Calculated from ICP. [b] Estimated by N_2 adsorption/desorption at 77 K. [c] BET surface area. [d] *t*-Plot. [e] ε_{1455} = 1.8 cm μmol^{-1}.[45] [f] ε_{1547} = 1.4 ± 0.2 cm μmol^{-1}.

using IR spectroscopy, and the corresponding IR spectra in the stretching OH spectral region between 3800 and 3500 cm^{-1} are shown in Fig. S2 (ESI†). Two major peaks are observed: the first ν_{OH} band at 3744 cm^{-1} corresponds to the silanol groups located on the outer surface of the crystallite.[53] The second, situated at 3610 cm^{-1} and absent in the IR spectrum of silicalite-1 (Fig. S2, ESI,† spectrum (a)), is attributed to structural bridged Si(OH)Al, namely Brønsted acid sites (BASs).[54] The absence of an additional vibrational band near 3665 cm^{-1} indicates that no vibrations of the OH groups bound to the extra-framework Al species are significantly present.[55,56] It should however be indicated that a small quantity is present in the MFI-11 sample because a small band can be guessed at around 3665 cm^{-1} on the corresponding IR spectrum.

Moreover, the morphology of the crystals is determined using scanning electron microscopy. SEM images (Fig. 2) reveal the aggregation of nanospheres of a size ranging between 30 and 100 nm for all zeolites and 1–2 μm for MFI-15. The SEM image of MFI-11 shows an agglomeration of nanosheets of less than 100 nm.

3.2. Accessibility of acid sites

The concentrations of both Brønsted and Lewis acid sites have been determined for each zeolite from pyridine adsorption using *in situ* FTIR spectroscopy. An excess of pyridine (1 torr at equilibrium pressure) sufficient to neutralize all acid sites was established in the IR cell at 150 °C, followed by evacuation under secondary vacuum at the same temperature to remove the gaseous and weakly physisorbed probe molecules. Finally, the corresponding spectra were recorded at RT to determine the number of acidic sites of each zeolite using the area of the 1547 cm^{-1} band of pyridinium ions (Brønsted) and the 1455 cm^{-1} band of pyridine coordinatively bonded to Lewis sites by applying their respective molar absorption coefficients. The subtraction spectra (before and after pyridine adsorption) are shown in Fig. 3(A) in the spectral region between 1700 and 1400 cm^{-1}. The quantities of adsorbed PyH^+ and PyL formed on the acidic sites are calculated using the Beer–Lambert law (eqn (1)) by measuring the area of the characteristic bands observed upon the interaction of pyridine with the acid sites on the subtracted spectra and using the calculated molar absorption coefficients (ε_{1455} and ε_{1547} are reported in Table 1). The obtained quantities are summarized in Table 1 for all MFI zeolites. The amount of Brønsted acid sites (BASs) clearly increases proportionally with the number of the Al content per unit cell. However, the amount of Lewis acid sites remains relatively low compared to that of the BASs. It is worth noticing that a such correlation is fully in agreement with the results of Agostini *et al.*[34] obtained by pyridine thermodesorption experiments on a series of MFI zeolites with various Si/Al ratios (Fig. S3, ESI†).

3.3. Determination of the molar absorption coefficients of adsorbed ethanol $\varepsilon\left(\delta_{EtOH}^{1450cm^{-1}}\right)$ and water and $\varepsilon\left(\delta_{H_2O}^{1630cm^{-1}}\right)$

Determining the molar absorption coefficients relative to the adsorbed water and alcohol is essential to convert the IR spectra into quantitative data. For this purpose, the adsorption of ethanol and water is investigated using IR spectroscopy and conducted using the AGIR setup for all MFI zeolites.

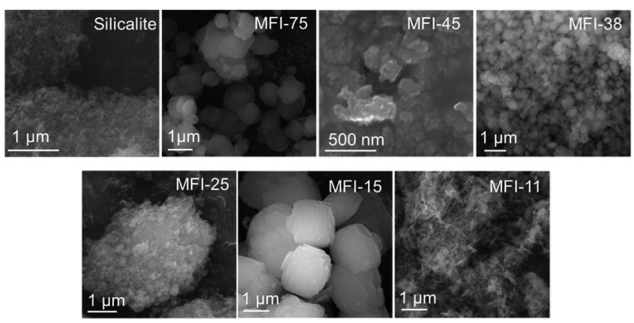

Fig. 2 SEM images of MFI samples with different Si/Al ratios.

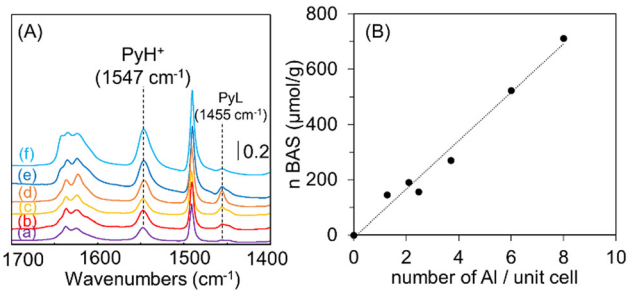

Fig. 3 (A) Subtraction IR spectra before and after pyridine adsorption for MFI-75 ((a), purple), MFI-45 ((b), red), MFI-38 ((c), yellow), MFI-25 ((d), orange), MFI-15 ((e), dark blue) and MFI-11 ((f), light blue). The spectra were collected at RT after pyridine adsorption at 150 °C and normalized to the mass of the pellet (20 mg). (B) Evolution of the amount of Brønsted acid sites as a function of the Al content per unit cell.

The experiments were repeated two times to check the reproducibility and the relative errors were estimated to be lower than 3%.

Typical IR spectra recorded at room temperature of adsorbed ethanol or water are displayed in Fig. 4(A) for the MFI-45 sample. The main characteristic vibrational bands of adsorbed ethanol are situated at 3000–2800 cm^{-1}, 1500–1350 cm^{-1}, and 880 cm^{-1} and are attributed to ν_{CH}, δ_{CH} and $\nu_{s(CCO)}$ modes, respectively. In the present study, only the band of ethanol at 1450 cm^{-1} (δ as $_{CH_3}$ mode) is considered: the ν_{CH} bands of ethanol at 3000–2800 cm^{-1} are intense, and the area is only measurable at low alcohol pressures, whereas the area of the band at 880 cm^{-1} is difficult to assess precisely due to the strong fluctuations and perturbation of the baseline ("*U*" shaped curve) by the structural bands of the zeolites.

In the case of H_2O, the main spectral bands observed at ~1630 cm^{-1} and ~5200 cm^{-1} are respectively assigned to the δ_{H_2O} and $(\delta + \nu)_{H_2O}$ vibration modes. Only the band at 1630 cm^{-1} is considered since the signal-to-noise ratio at ~5200 cm^{-1} at low water pressure is too low for the accurate integration of the band area.

The area of the characteristic band of ethanol $\left(\delta_{EtOH}^{1450cm^{-1}}\right)$ (Fig. 4(B)) at 1450 cm^{-1} and that of water $(\delta_{H_2O}^{1630cm^{-1}})$ situated at 1630 cm^{-1} (Fig. 4(C)) are plotted as a function of the quantities of the adsorbed species determined by gravimetric measurements. For the overall zeolites, molar absorption coefficients (ε (cm μmol^{-1})) are thus determined as proportional to the slope of the plot (ε = slope multiplied by 2.0 to take into account the area of the pellet) according to the Beer–Lambert law (eqn (1)):

$$A = \varepsilon \cdot l \cdot c = \varepsilon \cdot l \cdot \frac{n}{V} = \varepsilon \cdot l \cdot \frac{n}{l \cdot S} = \varepsilon \cdot \frac{n}{S} \quad (1)$$

where A (cm^{-1}) is the integrated area of the band, ε (cm μmol^{-1}) is the molar absorption coefficient, l (cm) is the optical pathway, c (μmol per volume unity) is the concentration of the adsorbate, V (cm^3) is the volume of the pellet, S (= 2.0 cm^2) is the surface of the pellet and n (μmol) is the amount of the adsorbate.

From the slope of the straight line, an average value for the molar absorption coefficients $\varepsilon\left(\delta_{EtOH}^{1450cm^{-1}}\right)$ and $\varepsilon\left(\delta_{H_2O}^{1630cm^{-1}}\right)$ is calculated and found to be equal to 0.14 ± 0.01 and 1.29 ± 0.06 cm μmol^{-1}, respectively. These values are found to be independent of the Si/Al ratio of the MFI zeolites.

3.4. Adsorption sites of ethanol or water on MFI-45

Ethanol and water are adsorbed separately on MFI-45. MFI-45 was chosen as the reference material to present in detail the spectroscopic study of water and ethanol adsorption experiments considering its intermediate Si/Al ratio (the concomitant presence of Si–OH and BASs).

3.4.1. Ethanol adsorption. The isotherms of ethanol adsorption with the corresponding IR spectra are shown in Fig. 5; at low ethanol partial pressures ($P/P_0 < 0.01$), ethanol is adsorbed to fill the porosity of the MFI zeolite (Fig. 5(A)-curve (a)). The corresponding IR spectra in the OH region are plotted in Fig. 5(B) and reveal that the ν_{OH} band at 3610 cm^{-1}, the characteristic of the BASs, disappears immediately after the first equilibrium pressure (P/P_0 = 0.0065). This observation agrees with the results obtained by Alexopoulos *et al.*[27] With the increase of the partial pressure, the quantity of adsorbed ethanol on MFI-45 increases to reach a maximum of around 2500 μmol g^{-1} at P/P_0 = 0.65. As suggested by Gómez-Álvarez *et al.*,[30] the zig–zag channels of the MFI structure are responsible for the high adsorption

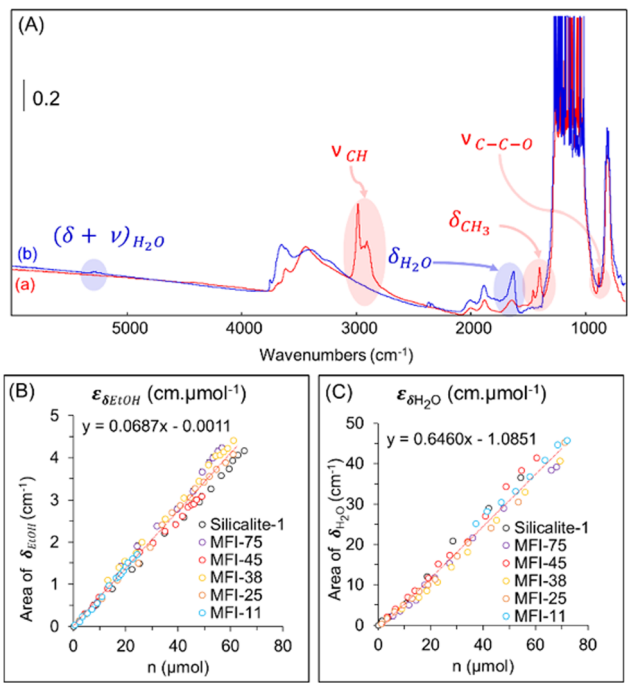

Fig. 4 (A) IR spectra of MFI-45 with the characteristic bands after ethanol ((a), red) and water ((b), blue) adsorption at RT. Evolution of the area of the characteristic band of (B) ethanol (1450 cm^{-1}) and (C) water (1630 cm^{-1}) as a function of the quantities adsorbed on silicalite-1 (black), MFI-75 (purple), MFI-45 (red), MFI-38 (yellow), MFI-25 (orange) and MFI-11 (light blue).

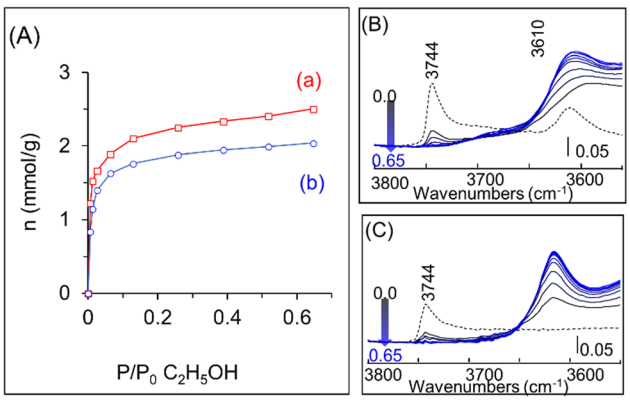

Fig. 5 (A) Gravimetric adsorption isotherms after C_2H_5OH adsorption on MFI-45 at RT ((a), red) without and ((b), blue) with pre-adsorbed lutidine. Evolution of the corresponding IR spectra at increasing partial pressures of C_2H_5OH in the spectral regions between the OH stretching region (3800–3550 cm^{-1}) (B) without and (C) with pre-adsorbed lutidine. The dashed spectra correspond to the initial spectra after activation at RT and before adsorption. Spectra are normalized to 20 mg of the zeolite.

capacity toward ethanol. The ethanol adsorption on MFI-45 occurs in a monolayer adsorption model, as previously described in the literature using a Langmuir model.[31] However, the concomitant decrease in the intensity of ν_{OH} at 3744 cm^{-1} assigned to external silanol groups at P/P_0 = 0.0065 shows that ethanol adsorption takes place also on the outer surface of the zeolite structure. This agrees with the results stating that ethanol highly interacts with the silanol groups of the MFI zeolites in the membrane.[57,58]

To elucidate the role of BASs on the adsorption sites of ethanol on MFI zeolites, ethanol is adsorbed on MFI-45 previously treated with lutidine, a basic probe molecule well-known to poison the BASs of the zeolites, specifically.[59,60] The spectra of MFI-45 before and after lutidine adsorption (Fig. S4, ESI†) show that the characteristic band of the Brønsted acid sites at 3610 cm^{-1} disappears after introducing lutidine. In contrast, the bands of lutidinium at 1630 and 1650 cm^{-1} are well detected, showing the blockage of the BASs before ethanol adsorption. The gravimetric isotherms after ethanol adsorption in the presence of lutidine and the corresponding IR spectra in the OH region are shown in Fig. 5 and compared to the gravimetric adsorption isotherms of the lutidine free parent MFI zeolite. A slight decrease in the ethanol adsorbed quantity was observed (around 20%) (Fig. 5(A)-curve (b)). After adsorbing ethanol, the characteristic vibrational band at 3744 cm^{-1} is highly affected at very low ethanol partial pressures in the presence of lutidine (Fig. 5(C)). Its intensity decreases with the increase of the partial pressure. Based on these results, we can assume that the adsorption of ethanol takes place on the silanol groups since a slight decrease in the quantity of adsorbed ethanol is observed after blocking the BASs. In addition, the number of adsorbed ethanol molecules per Brønsted acid site could be determined from the subtraction between the gravimetric isotherms before and after adsorbing lutidine. The difference suggests that two ethanol molecules are adsorbed on the BAS, agreeing with the data in the literature[27] (for example, at P/P_0 = 0.65, the difference in adsorbed EtOH is 468 μmol g^{-1}, and the number of BAS is equal to 235 μmol g^{-1}, *i.e.*, an EtOH/BAS ratio equal to ~2). Note that the number of BASs evaluated using lutidine is slightly higher than that determined using pyridine (Table 1), however not affecting the EtOH/BAS ratio. This difference may be due to the measurement accuracies and/or to the stronger basicity of lutidine which can thus probes a few amount of additional weaker Brønsted acid sites.

3.4.2. Water adsorption. The isotherm of water adsorption over MFI-45 is displayed in Fig. 6(A)-curve (a), and the corresponding IR spectra are shown in Fig. 6(B). The band of the BASs at 3610 cm^{-1} disappears at the first water uptake (P/P_0 = 0.01), whereas the intensity of the SiOH groups at 3744 cm^{-1} is weakly affected and subsequently decreases significantly only at P/P_0 up to 0.04. This suggests that water molecules interacts specifically with BASs at low partial pressures.[61] While the sensitivity of the ν_{OH} band of BASs upon water and ethanol adsorption is similar, this is not the case for the ν_{OH} band of silanol, much more affected upon ethanol adsorption.[27,31,62] This can be explained

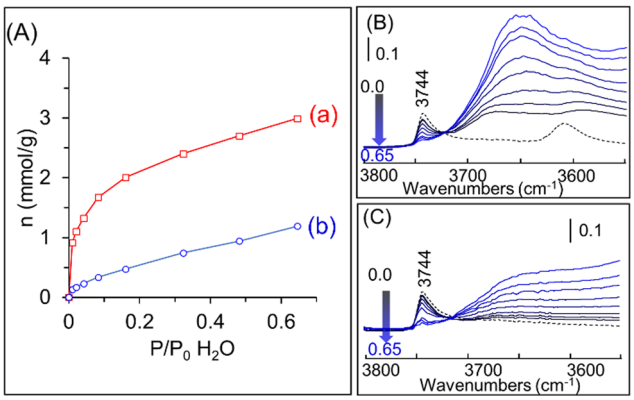

Fig. 6 (A) Gravimetric adsorption isotherms after H_2O adsorption on MFI-45 at RT ((a), red) without and ((b), blue) with pre-adsorbed lutidine. Evolution of the corresponding IR spectra at increasing partial pressures of H_2O in the spectral regions between the OH stretching regions (3800–3550 cm^{-1}) (B) without and (C) with pre-adsorbed lutidine. The dashed spectra correspond to the initial spectra after activation at RT and before H_2O adsorption. Spectra are normalized to 20 mg of the zeolite.

considering the difference of affinity toward ethanol and water, *e.g.*, the enthalpies of adsorption. The enthalpy of ethanol adsorption is higher than that of water and is characterized by two plateaus. Whereas that of water is characterized by a single plateau attributed to the clustering of water molecules.[63] Water molecules are first adsorbed on the Brønsted acid sites, and then strong interactions occur between the adsorbed water molecules and the second water molecules.[64]

Water adsorption sites are further studied after adsorbing lutidine. The gravimetric isotherm of water adsorption on MFI-45 with pre-adsorbed lutidine and the corresponding IR spectra in the OH region are shown in Fig. 6(A) and (C). By comparing the gravimetric isotherms, the quantity of adsorbed water on MFI-45 without lutidine is more important than that on MFI-45 filled with lutidine. After adsorbing water, a minor decrease of the vibrational band at 3744 cm^{-1} is observed at a water partial pressure $0 < P/P_0 < 0.16$. At higher partial pressures, an important decrease in the intensity of the characteristic bands of silanols is observed. These observations allow us to confirm the strong adsorption of water molecules on BASs and their weak interactions with the silanol groups.[65,66] Moreover, the difference between the adsorption isotherms of water with and without lutidine demonstrates that four water molecules are adsorbed on one BAS at a low water partial pressure ($P/P_0 \leq$ 0.02). For example, at P/P_0 = 0.02, the difference in adsorbed water is 931 μmol/g, and the number of BASs is equal to 235 μmol/g, *i.e.*, an H_2O/BAS ratio is equal to ~4). Similar results were obtained by Olson *et al.*[32,67] and Bolis *et al.*[66]

3.5. Adsorption of ethanol or water on MFI zeolites with different Si/Al ratios

The adsorption of ethanol and water is further investigated on MFI zeolites with different Si/Al ratios. The gravimetric isotherms of ethanol and water are determined from the AGIR setup and are shown in Fig. 7. The corresponding IR spectra at fixed partial pressures are shown in Fig. S5 (ESI†). The quantity

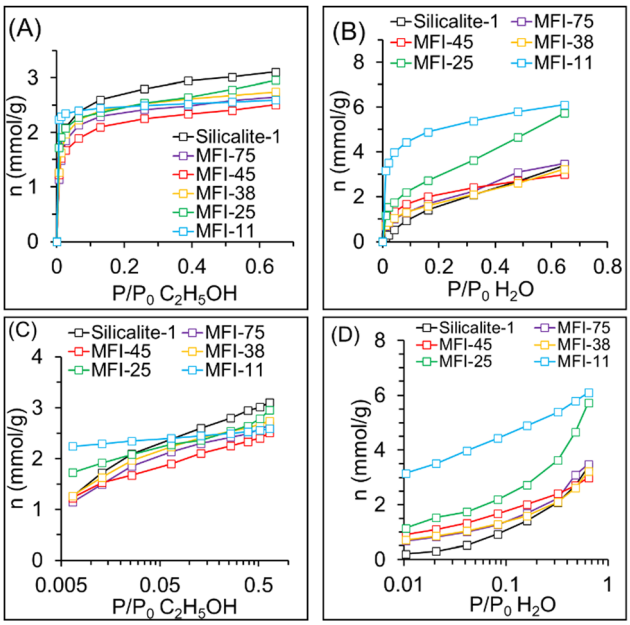

Fig. 7 Adsorption isotherms of (A) ethanol and (B) water on silicalite-1 (black), MFI-75 (purple), MFI-45 (red), MFI-38 (yellow), MFI-25 (green), and MFI-11 (light blue). Semi-log plot of the adsorption isotherms of (C) ethanol and (D) water.

of adsorbed ethanol increases until reaching an equilibrium at P/P_0 = 0.3. At P/P_0 > 0.3, the quantity of adsorbed ethanol increases slightly to reach a maximum ranging between 2400 and 3100 μmol/g. Ethanol adsorption isotherms follow a similar adsorption type regardless of the Si/Al ratio. A Langmuir-like model can be observed, where the organophilic character of MFI zeolites is responsible for the monolayer adsorption of ethanol. These results agree with the results previously reported in the literature.[31] The effect of the Si/Al ratio is mainly observed at low ethanol partial pressures (P/P_0 < 0.01) (Fig. 7(C)), where zeolites with low Si/Al ratios adsorb the highest ethanol quantity.

A different trend is observed after water adsorption (Fig. 7(B) and (D)). First, all zeolites exhibit a Freundlich-like isotherm upon water adsorption, where different layers of adsorbed water are formed.[64] On silicalite-1 and MFI zeolites with relatively high Si/Al ratios, the quantity of adsorbed water varies in the same range between 2700 and 3300 μmol g^{-1}. However, at a lower Si/Al ratio, for MFI-25 and MFI-11, a significant increase in water adsorption capacity is observed. The adsorbed water quantity at P/P_0 = 0.64 reaches 6100 μmol g^{-1}. These differences are attributed to the change of the hydrophobic character of zeolites due to the presence of Al in the framework.[31,32] The presence of Al is responsible for creating Brønsted acid sites in the framework (Table 1), considered as the adsorption sites for water. As a result, the hydrophobic character of the zeolite decreases, thus increasing the adsorption capacity of water. This adsorption model is also confirmed by the linear correlation between the number of BASs determined by pyridine adsorption and the quantity of adsorbed water at relatively low partial pressures (P/P_0= 0.0065) (Fig. S6, ESI†). The linear correlation between the quantities of these adsorbed species and the number of Brønsted acid sites determined by pyridine adsorption allows us to determine the number of adsorbed molecules per acid site for each adsorbate at each partial pressure. The slope of the linear correlation (Fig. S6, ESI†) indicates that approximately four water molecules are adsorbed at saturation on the Brønsted acid sites. These results are consistent with the previously demonstrated results on MFI-45 after the adsorption of lutidine. Whereas for ethanol, the number of adsorbed ethanol is only determined upon lutidine adsorption (about two molecules per BAS).

3.6. Coadsorption of ethanol and water on MFI zeolites with different Si/Al ratios

3.6.1. Validation of the $\varepsilon\left(\delta_{EtOH}^{1450cm^{-1}}\right)$ and $\varepsilon\left(\delta_{H_2O}^{1630cm^{-1}}\right)$ values for coadsorption experiments: comparison between the AGIR and Carroucell setups. The coadsorption of ethanol and water on the MFI zeolites with different Si/Al ratios was conducted on the Carroucell setup, as previously described in the Experimental section. A single experiment was conducted first on the AGIR setup on MFI-45 to confirm that the molar absorption coefficients determined during pure ethanol and water adsorption experiments do not change during their coadsorption. Water is initially adsorbed on the zeolite, and when the equilibrium is reached, the gas flow is enriched with an increasing concentration of ethanol. The IR spectra of MFI-45 recorded using the Carroucell at different P/P_0 of C_2H_5OH and at a fixed H_2O concentration (P/P_0 = 0.32) are reported in Fig. 8 (B). Initially, in the absence of EtOH, only the peak at ~1630 cm^{-1} characteristic of adsorbed water is present. Subsequently, the step-by-step increase in the partial pressure P/P_0 of C_2H_5OH leads to a decrease in the intensity of the δH_2O band and to the concomitant increase of the characteristic bands of the adsorbed alcohol, in particular, the one at 1450 cm^{-1}. The molar absorption coefficients previously determined from the AGIR setup are used to determine the quantities of each adsorbed species from the IR

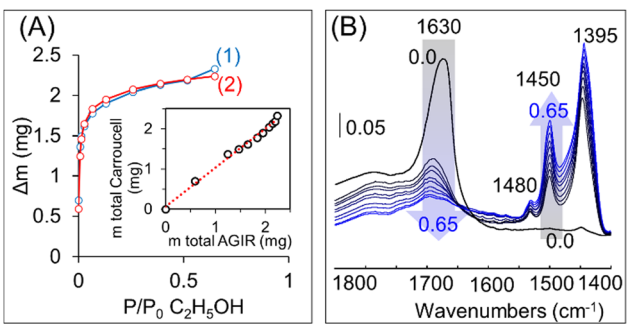

Fig. 8 (A) Mass variation (Δm, mg) as a function of increasing P/P_0 of C_2H_5OH determined using the Carroucell ((1), blue)) and using AGIR ((2), red). (B) Evolution of the IR spectra of MFI-45 recorded using the Carroucell at an increasing P/P_0 of C_2H_5OH and a fixed H_2O concentration (P/P_0 = 0.32). The spectra correspond to the subtracted spectrum between the spectra after activation recorded at RT and the successive spectra recorded at RT at equilibrium after C_2H_5OH/H_2O adsorption. The inset of (A) shows the linear correlation between the total mass calculated from the Carroucell and the AGIR.

spectra recorded using the Carroucell. Finally, the calculated total quantity of ethanol and water adsorbed on the zeolite *via* the Carroucell is compared to the mass uptake recorded using the microbalance of the AGIR setup (Fig. 8(A)). The results show that the quantities of adsorbed ethanol and water are similar, as demonstrated by the linear correlation obtained between the total adsorbed quantities determined using the AGIR tool and the Carroucell *via* the molar absorption coefficients, respectively (the inset in Fig. 8(A)). Thus, we conclude that the molar absorption coefficient of each adsorbate is not significantly affected by the presence of the second species. Consequently, the Carroucell set-up can be used to drastically reduce the experimental time while rigorously reproducing the same conditions (temperature and pressure) since the experiment is carried out simultaneously for all the samples placed under the same environmental conditions.

3.6.2. Ethanol/water selectivity. The selectivity of ethanol over water is strongly related to the hydrophobic/hydrophilic properties of MFI zeolites and then to the Si/Al ratio.[30] This selectivity ($S_{C_2H_5OH,H_2O}$) is defined according to the following equation:

$$S_{C_2H_5OH,\,H_2O} = \frac{\frac{x_{C_2H_5OH}}{y_{C_2H_5OH}}}{\frac{x_{H_2O}}{y_{H_2O}}} \quad (2)$$

where x and y correspond to the molar fractions of water or ethanol in the adsorbed and vapor phases, respectively.

The selectivity factor has been determined at increasing ethanol partial pressures (P/P_0 = 0.006–0.52) at a water vapor partial pressure of P/P_0 = 0.16. It is noted that some of the selectivity values are not reported due to uncertainties in the calculated values for the previously studied MFI zeolites. The $S_{C_2H_5OH,H_2O}$ values are reported in Fig. 9 for silicalite-1, MFI-45, MFI-25, and MFI-11 at P/P_0 H_2O = 0.16, with an increasing P/P_0 of ethanol. It is observed that the ethanol selectivity decreases with the increase of P/P_0 C_2H_5OH for all the zeolites and is always greater than 1 for silicalite-1, MFI-45, and MFI-25, suggesting selective ethanol adsorption even at a low P/P_0 of C_2H_5OH for the highest siliceous zeolite samples. However, the $S_{C_2H_5OH,H_2O}$ value is less than 1 for MFI-11 at high ethanol partial pressures indicating preferential water adsorption.

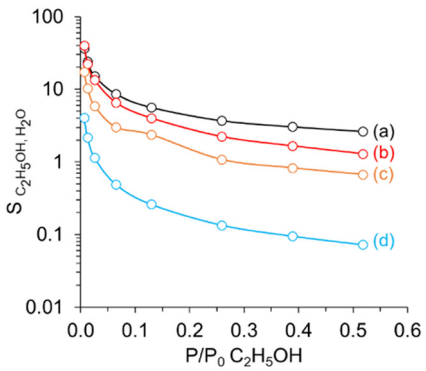

Fig. 9 Selectivity of C_2H_5OH determined on silicalite-1 ((a), black), MFI-45 ((b), red), MFI-25 ((c), orange) and MFI-11 ((d), light blue) at fixed P/P_0 = H_2O (0.16) and increasing P/P_0 C_2H_5OH.

Comparing the selectivity between the four samples at a given ethanol partial pressure (for example, at P/P_0 = 0.26) shows that the ethanol sorption selectivity decreases with the decrease of the Si/Al ratio. Yet, it decreases drastically when comparing silicalite-1 (Fig. 9 curve (a)) and MFI-11 (Fig. 9 curve (d)). Hence, MFI-11, the highest Al content zeolite, is highly selective for adsorbing water toward ethanol. It is concluded that the lower the Si/Al ratio, the higher the zeolite hydrophilicity is, and then water is strongly adsorbed in the zeolite and is not easily replaced by ethanol. The effect of the Si/Al ratio on the selectivity of ethanol over water is in agreement with the results reported in the literature,[31,68] extending this conclusion to a larger Si/Al range and at different partial pressures.

3.6.3. Influence of the Si/Al ratio and the fraction of H_2O in the gas phase on the relative amount of adsorbed EtOH ($R_{C_2H_5OH}$). The area of the vibrational band of water at 1630 cm^{-1} cannot always be measured precisely for all zeolites for small amounts of adsorbed H_2O due to the distortion of the baseline in this range (distortion resulting mainly from the shift of the underlying combination and overtone bands of ν_{Si-O} structural vibrations). This is why we have chosen to introduce a new factor independent of the measurement of the quantity of coadsorbed water in order to compare the ethanol adsorption capacities of the overall zeolites with and without water. Hence, the selective adsorption of ethanol is interpreted after introducing a new variable, the ratio of adsorbed ethanol ($R_{C_2H_5OH}$). It is determined, at a constant ethanol partial pressure, as the ratio of the adsorbed ethanol quantities in the presence ($(Q_{C_2H_5OH})^{P/P_0H_2O}_{P/P_0C_2H_5OH}$) and absence ($(Q_{C_2H_5OH})^{0}_{P/P_0C_2H_5OH}$) of water, respectively, as reported in eqn (3):

$$(R_{C_2H_5OH})_{P/P_0C_2H_5OH} = \frac{(Q_{C_2H_5OH})^{P/P_0H_2O}_{P/P_0C_2H_5OH}}{(Q_{C_2H_5OH})^{0}_{P/P_0C_2H_5OH}} \times 100 \quad (3)$$

The ratio of adsorbed ethanol ($R_{C_2H_5OH}$) is plotted as a function of the number of Al atoms per unit cell for different ethanol partial pressures at four different water partial pressures (Fig. 10 and Fig. S7, ESI†). For a fixed water vapor concentration, for example, at P/P_0 = 0.16, the ratio of adsorbed ethanol decreases with the increase of the number of Al per unit cell, regardless of the ethanol partial pressure. At low

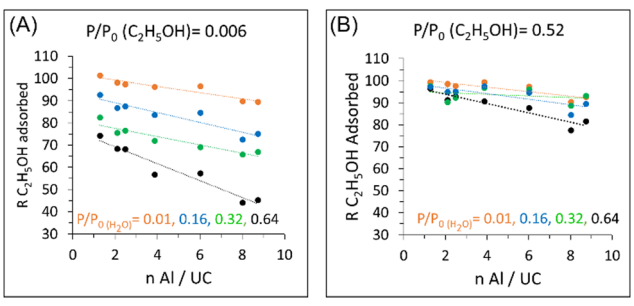

Fig. 10 Ratio of adsorbed C_2H_5OH *vs* the number of Al per unit cell at P/P_0 C_2H_5OH = 0.006 (A) and 0.52 (B) after the adsorption of different water partial pressures (P/P_0 H_2O = 0.01 (orange), P/P_0 H_2O = 0.16 (blue), P/P_0 H_2O = 0.32 (green) and P/P_0 H_2O = 0.64 (black)) for different MFI zeolites.

ethanol partial pressures (P/P_0 = 0.006) (Fig. 10(A)), the ratio of adsorbed ethanol decreases with the increase of the number of Al for a fixed water content. A dramatic difference between the ratios of adsorbed ethanol is observed when the initial water content increases at low ethanol concentrations for a fixed number of Al per unit cell. Nevertheless, this trend is not observed when the ethanol concentration is close to saturation (P/P_0 = 0.52), although the ratio of adsorbed C_2H_5OH keeps decreasing with the increase of the number of Al per unit cell (Fig. 10(B)). This demonstrates the clear effect of water on ethanol adsorption at low pressures and not at high pressures.

Finally, the color map visualization on Fig. 11 represents the ratio of adsorbed C_2H_5OH determined from the totality of ethanol/water coadsorption configurations previously studied at different partial pressures and Si/Al ratios. To make this map and in order to reduce the effect of the dispersion of experimental data, a polynomial curve fitting (order 3) has been determined for each zeolite considering all the experimental data relative to $R_{C_2H_5OH}$ *versus* the molar percentage of H_2O (in the gas phase). Fig. 11 clearly shows the effects of both the Si/Al ratio and the water content in the gas phase on ethanol adsorption. The adsorption of ethanol is less affected by water at low water content (the dark part of the map). With the increase of the water content in the gas phase, ethanol is less adsorbed, regardless of the Si/Al ratio (light area). Moreover, ethanol is highly adsorbed on high Si/Al ratio zeolites. These results are in good agreement with other studies claiming that the selectivity of ethanol increases with the increase of the Si/Al ratio and the total flux.[31,69] But unlike these studies which link the activity of zeolitic materials to their Si/Al ratios, our study is directly based on the measured values of adsorbed water and ethanol determined from IR spectra also highlighting the different adsorption sites such as silanol and BASs. Therefore, the Si/Al ratio and the water content directly impact the ethanol sorption properties and govern the choice of the mixed membranes to separate bioethanol from its aqueous mixture.

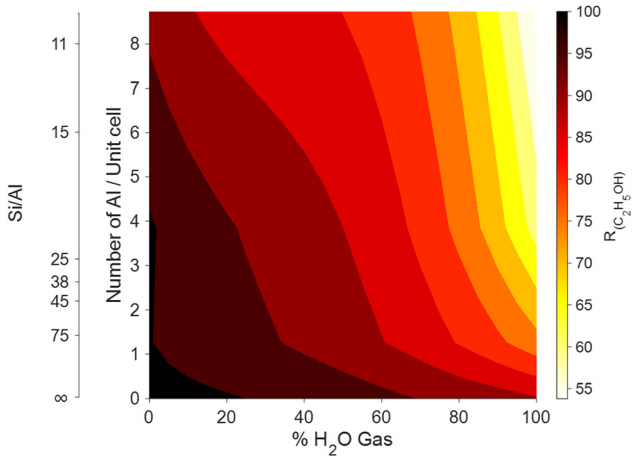

Fig. 11 Ratio of adsorbed C_2H_5OH as a function of the number of Al per unit cell, the Si/Al ratio, and the percentage of H_2O in the gas phase. Note that the adsorption of pure ethanol at 0% H_2O is not included in the figure to avoid mathematical problems in fitting the graph.

4. Conclusions

The use of advanced vibrational spectroscopic tools allows obtaining quantitative data for ethanol and water adsorption and coadsorption on MFI zeolites with different Si/Al ratios. The use of a high-throughput IR cell like the CARROUCELL for this type of study has been very beneficial for (1) making it easier to compare several samples since they are simultaneously subjected to exactly the same experimental conditions (temperature, partial pressures, *etc.*) in a common chamber and (2) increasing both the sensitivity and the extent of the experimental conditions because a large number of different experimental conditions (temperature and partial pressures of water and ethanol) can be used in a very reasonable time. The correlation between the gravimetric analysis and the evolution of the characteristic spectroscopic bands of the adsorbed ethanol or water using the AGIR system leads to the determination of the molar absorption coefficients of adsorbed species. They are equal to 0.14 ± 0.01 and 1.29 ± 0.06 cm μmol^{-1}, respectively, and are independent of the Si/Al ratio whether adsorbed or coadsorbed.

Gravimetric-IR coupled experiments reveal that water adsorbs preferentially on BASs at low partial pressures, whereas ethanol adsorbs on both silanol and BASs. The number of adsorbed molecules per Brønsted acid site is estimated to be four water molecules and two ethanol molecules per acid site.

The Si/Al ratio effect was further studied and significantly affected ethanol adsorption isotherms only at low partial pressures. However, a significant effect on the amount of adsorbed water is evidenced at an extended water partial pressure, demonstrating its effect on the hydrophobic character of the material.

The use of molar absorption coefficients of adsorbed water and ethanol allows obtaining an important data set relative to the concentration of ethanol and water from the binary adsorption measurements, using the developed multi-sample *in situ* IR cell (CARROUCELL). Finally, the water molar fraction in the gas phase plays a significant role in ethanol adsorption, leading to lower adsorption capacity at a high water content. Furthermore, a higher Si/Al ratio leads to higher ethanol adsorption capacity in the presence of water. This work offers valuable insights into studying other mixtures' adsorption mechanisms using IR spectroscopy.

Author contributions

The manuscript was written with the contributions of all authors. All authors have approved the final version of the manuscript.

Conflicts of interest

There are no conflicts of interest to declare.

Acknowledgements

R. Zakhia Douaihy acknowledges the Normandy region for the doctoral funding (RIN doctorant). The authors acknowledge Dr Jaafar El Fallah for helping in the SEM analysis.

References

1 J. J. Cheng and G. R. Timilsina, *Renewable Energy*, 2011, **36**, 3541–3549.
2 V. G. Gude and E. Martinez-Guerra, *Environ. Chem. Lett.*, 2018, **16**, 327–341.
3 R. K. Malhotra and L. M. Das, *J. Sci. Ind. Res.*, 2003, **62**, 90–96.
4 S. A. Jambo, R. Abdulla, S. H. M. Azhar, H. Marbawi, J. A. Gansau and P. Ravindra, *Renewable Sustainable Energy Rev.*, 2016, **65**, 756–769.
5 S. K. Chauhan, S. Gangopadhyay and N. Singh, *Environ. Chem. Lett.*, 2009, **7**, 289–299.
6 S. Karimi, R. R. Karri, M. T. Yaraki and J. R. Koduru, *Environ. Chem. Lett.*, 2021, 1–18.
7 C. R. Soccol, V. Faraco, S. G. Karp, L. P. Vandenberghe, V. Thomaz-Soccol, A. L. Woiciechowski and A. Pandey, *Biofuels: Alternative Feedstocks and Conversion Processes for the Production of Liquid and Gaseous Biofuels*, Elsevier, 2019, pp. 331–354.
8 A. S. Kumar, S. S. Sankar, S. Godlaveeti, D. Kumar, S. Dheiver, R. Prasad, C. Nb, T. H. C. Nguyen and Q. Van Le, *Bioenergy Res.*, 2021, 175–208.
9 T. J. Tse, D. J. Wiens and M. J. Reaney, *Fermentation*, 2021, **7**, 268.
10 S. Karimi, M. T. Yaraki and R. R. Karri, *Renewable Sustainable Energy Rev.*, 2019, **107**, 535–553.
11 S. Kumar, N. Singh and R. Prasad, *Renewable Sustainable Energy Rev.*, 2010, **14**, 1830–1844.
12 X. Liu, D. Hu, M. Li, J. Zhang, Z. Zhu, G. Zeng, Y. Zhang and Y. Sun, *J. Appl. Polym. Sci.*, 2015, **132**, 42460–42471.
13 M. El-Roz, P. Bazin, T. B. Čelič, N. Z. Logar and F. Thibault-Starzyk, *J. Phys. Chem. C*, 2015, **119**, 22570–22576.
14 S. Mintova, J.-P. Gilson and V. Valtchev, *Nanoscale*, 2013, **5**, 6693–6703.
15 N. Kosinov, J. Gascon, F. Kapteijn and E. J. Hensen, *J. Membr. Sci.*, 2016, **499**, 65–79.
16 L. Bacakova, M. Vandrovcova, I. Kopova and I. Jirka, *Biomater. Sci.*, 2018, **6**, 974–989.
17 M. Moshoeshoe, M. S. Nadiye-Tabbiruka and V. Obuseng, *Am. J. Mater. Sci.*, 2017, **7**, 196–221.
18 J. A. Delgado, M. A. Uguina, J. L. Sotelo, V. I. Águeda, A. García and A. Roldán, *Chem. Eng. J.*, 2012, **180**, 137–144.
19 J. Laksmono, I. Pratiwi, M. Sudibandriyo, A. Haryono and A. H. Saputra, *AIP Conf. Proc.*, 2017, **1904**, 020076.
20 M. Simo, S. Sivashanmugam, C. J. Brown and V. Hlavacek, *Ind. Eng. Chem. Res.*, 2009, **48**, 9247–9260.
21 J. I. Siepmann, P. Bai and M. Tsapatsis, *Zeolites for separation of ethanol and water*, University of Minnesota, Minneapolis, MN (United States), 2018.
22 H. Zhou, J. Mouzon, A. Farzaneh, O. N. Antzutkin, M. Grahn and J. Hedlund, *Langmuir*, 2015, **31**, 8488–8494.
23 R. F. DeJaco, P. Bai, M. Tsapatsis and J. I. Siepmann, *Langmuir*, 2016, **32**, 2093–2101.
24 K. Zhang, R. P. Lively, M. E. Dose, L. Li, W. J. Koros, D. M. Ruthven, B. A. McCool and R. R. Chance, *Microporous Mesoporous Mater.*, 2013, **170**, 259–265.
25 S.-i Furukawa, K. Goda, Y. Zhang and T. Nitta, *J. Chem. Eng. Jpn.*, 2004, **37**, 67–74.
26 Q. Shi, Z. He, K. M. Gupta, Y. Wang and R. Lu, *J. Mater. Sci.*, 2017, **52**, 173–184.
27 K. Alexopoulos, M.-S. Lee, Y. Liu, Y. Zhi, Y. Liu, M.-F. O. Reyniers, G. B. Marin, V.-A. Glezakou, R. Rousseau and J. A. Lercher, *J. Phys. Chem. C*, 2016, **120**, 7172–7182.
28 D. Bastani, N. Esmaeili and M. Asadollahi, *J. Ind. Eng. Chem.*, 2013, **19**, 375–393.
29 J. P. Pariente and M. M. Sánchez, *Zeolites and ordered porous solids: fundamentals and applications*, Editorial Universitat Politècnica de València, 2011.
30 P. Gomez-Alvarez, E. G. Noya, E. Lomba, S. Valencia and J. O. Pires, *Langmuir*, 2018, **34**, 12739–12750.
31 K. Zhang, R. P. Lively, J. D. Noel, M. E. Dose, B. A. McCool, R. R. Chance and W. J. Koros, *Langmuir*, 2012, **28**, 8664–8673.
32 D. Olson, W. Haag and W. Borghard, *Microporous Mesoporous Mater.*, 2000, **35**, 435–446.
33 Y. Oumi, A. Miyajima, J. Miyamoto and T. Sano, *Studies in Surface Science and Catalysis*, Elsevier, 2002, vol. 142, pp. 1595–1602.
34 C. D'Agostino, R. D. Armstrong, G. J. Hutchings and L. F. Gladden, *ACS Catal.*, 2018, **8**, 7334–7339.
35 C. D'Agostino, S. Chansai, I. Bush, C. Gao, M. D. Mantle, C. Hardacre, S. L. James and L. F. Gladden, *Catal. Sci. Technol.*, 2016, **6**, 1661–1666.
36 V. I. Volkov, S. A. Korotchkova, H. Ohya and Q. Guo, *J. Membr. Sci.*, 1995, **100**, 273–286.
37 V. I. Volkov, V. D. Skirda, E. N. Vasina, S. A. Korotchkova, H. Ohya and K. Soontarapa, *J. Membr. Sci.*, 1998, **138**, 221–225.
38 F. Dreisbach, H. W. Lösch and K. Nakai, *Chem. Eng. Technol.*, 2001, **24**, 1001–1005.
39 R. Krishna and J. M. van Baten, *ACS Omega*, 2020, **5**, 28393–28402.
40 P. Gomez-Alvarez, E. G. Noya, E. Lomba, S. Valencia and J. Pires, *Langmuir*, 2018, **34**, 12739–12750.
41 A. Vimont, F. Thibault-Starzyk and M. Daturi, *Chem. Soc. Rev.*, 2010, **39**, 4928–4950.
42 E. Payen, J. Grimblot, J. Lavalley, M. Daturi and F. Mauge, Applications in industry, materials and the physical sciences, in *Handbook of Vibrational Spectroscopy*, ed. J. M. C. a. P. R. Griffith, Wiley, 2001, vol. 4, pp. 3005–3041.
43 P. Bräuer, P. L. Ng, O. Situmorang, I. Hitchcock and C. D'Agostino, *RSC Adv.*, 2017, **7**, 52604–52613.
44 P. Bräuer, O. Situmorang, P. L. Ng and C. D'Agostino, *Phys. Chem. Chem. Phys.*, 2018, **20**, 4250–4262.
45 V. Zholobenko, C. Freitas, M. Jendrlin, P. Bazin, A. Travert and F. Thibault-Starzyk, *J. Catal.*, 2020, **385**, 52–60.
46 R. Z. Douaihy, H. Nasrallah, O. Lebedev, J. El Fallah, R. Guillet-Nicolas, A. Vimont, P. Bazin and E.-R. Mohamad, *Mater. Chem. Phys.*, 2023, **293**, 126921.
47 P. Bazin, A. Alenda and F. Thibault-Starzyk, *Dalton Trans.*, 2010, **39**, 8432–8436.
48 J.-Y. Wang, E. Mangano, S. Brandani and D. M. Ruthven, *Adsorption*, 2021, **27**, 295–318.

49 L. Lakiss, I. Yordanov, G. Majano, T. Metzger and S. Mintova, *Thin Solid Films*, 2010, **518**, 2241–2246.
50 S. Jolly, J. Saussey, M. Bettahar, J. Lavalley and E. Benazzi, *Appl. Catal., A*, 1997, **156**, 71–96.
51 Z. Qin, L. Lakiss, L. Tosheva, J. P. Gilson, A. Vicente, C. Fernandez and V. Valtchev, *Adv. Funct. Mater.*, 2014, **24**, 257–264.
52 M. Thommes, K. Kaneko, A. V. Neimark, J. P. Olivier, F. Rodriguez-Reinoso, J. Rouquerol and K. S. Sing, *Pure Appl. Chem.*, 2015, **87**, 1051–1069.
53 F. Thibault-Starzyk, A. Vimont and J.-P. Gilson, *Catal. Today*, 2001, **70**, 227–241.
54 P. Peng, D. Stosic, A. Aitblal, A. Vimont, P. Bazin, X.-M. Liu, Z.-F. Yan, S. Mintova and A. Travert, *ACS Catal.*, 2020, **10**, 6822–6830.
55 S. Khabtou, T. Chevreau and J. Lavalley, *Microporous Mater.*, 1994, **3**, 133–148.
56 P. O. Fritz and J. H. Lunsford, *J. Catal.*, 1989, **118**, 85–98.
57 Z. Wu, C. Zhang, L. Peng, X. Wang, Q. Kong and X. Gu, *ACS Appl. Mater. Interfaces*, 2018, **10**, 3175–3180.
58 M. Selvaraj and F. Banat, *Biorefinery*, Springer, 2019, pp. 211–232.
59 F. Thibault-Starzyk, I. Stan, S. Abelló, A. Bonilla, K. Thomas, C. Fernandez, J.-P. Gilson and J. Pérez-Ramírez, *J. Catal.*, 2009, **264**, 11–14.
60 P. A. Jacobs and C. Heylen, *J. Catal.*, 1974, **34**, 267–274.
61 L. M. Parker, D. M. Bibby and G. R. Burns, *Zeolites*, 1993, **13**, 107–112.
62 G. Piccini, M. Alessio and J. Sauer, *Phys. Chem. Chem. Phys.*, 2018, **20**, 19964–19970.
63 D. Wu, X. Guo, H. Sun and A. Navrotsky, *J. Phys. Chem. C*, 2015, **119**, 15428–15433.
64 A. Jentys, G. Warecka, M. Derewinski and J. A. Lercher, *J. Phys. Chem.*, 1989, **93**, 4837–4843.
65 A. Vjunov, M. Wang, N. Govind, T. Huthwelker, H. Shi, D. Mei, J. L. Fulton and J. A. Lercher, *Chem. Mater.*, 2017, **29**, 9030–9042.
66 V. Bolis, C. Busco and P. Ugliengo, *J. Phys. Chem. B*, 2006, **110**, 14849–14859.
67 D. Olson, S. Zygmunt, M. Erhardt, L. Curtiss and L. Iton, *Zeolites*, 1997, **18**, 347–349.
68 K. Ueno, H. Negishi, M. Miyamoto, S. Uemiya and Y. Oumi, *Microporous Mesoporous Mater.*, 2018, **267**, 1–8.
69 X. Zhan, J.-d Li, J. Chen and J.-q Huang, *Chin. J. Polym. Sci.*, 2009, **27**, 771–780.